Anisotropy and temperature dependence of structural, thermodynamic, and elastic properties of crystalline cellulose I: a first-principles investigation

2014 Modelling Simul. Mater. Sci. Eng. 22 085012

(http://iopscience.iop.org/0965-0393/22/8/085012)

IOP Publishing Modelling and Simulation in Materials Science and Engineering

Modelling Simul. Mater. Sci. Eng. **22** (2014) 085012 (28pp) doi:10.1088/0965-0393/22/8/085012

Anisotropy and temperature dependence of structural, thermodynamic, and elastic properties of crystalline cellulose I_β: a first-principles investigation

Fernando L Dri[1], ShunLi Shang[2], Louis G Hector Jr[3], Paul Saxe[4], Zi-Kui Liu[2], Robert J Moon[5,6] and Pablo D Zavattieri[1]

[1] Lyles School of Civil Engineering, Purdue University, West Lafayette, IN 47907, USA
[2] Department of Materials Science and Engineering, The Pennsylvania State University, University Park, PA 16802, USA
[3] Chemical and Materials Systems Laboratory, General Motors Research and Development Center, Warren, MI 48090, USA
[4] Materials Design, Inc., Angel Fire, NM 87501, USA
[5] School of Materials Engineering and Birck Nanotechnology Center, Purdue University, West Lafayette, IN 47907, USA
[6] USDA Forest Service, Forest Products Laboratory, Madison, WI 53726, USA

E-mail: zavattie@purdue.edu (P D Zavattieri)

Received 21 May 2014, revised 6 September 2014
Accepted for publication 19 September 2014
Published 12 November 2014

Abstract

Anisotropy and temperature dependence of structural, thermodynamic and elastic properties of crystalline cellulose I_β were computed with first-principles density functional theory (DFT) and a semi-empirical correction for van der Waals interactions. Specifically, we report the computed temperature variation (up to 500 K) of the monoclinic cellulose I_β lattice parameters, constant pressure heat capacity, C_p, entropy, S, enthalpy, H, the linear thermal expansion components, ξ_i, and components of the isentropic and isothermal (single crystal) elastic stiffness matrices, $C_{ij}^S(T)$ and $C_{ij}^T(T)$, respectively. Thermodynamic quantities from phonon calculations computed with DFT and the supercell method provided necessary inputs to compute the temperature dependence of cellulose I_β properties via the quasi-harmonic approach. The notable exceptions were the thermal conductivity components, λ_i (the prediction of which has proven to be problematic for insulators using DFT) for which the reverse, non-equilibrium molecular dynamics approach with a force field was applied. The extent to which anisotropy of Young's modulus and Poisson's ratio is temperature-dependent was explored in terms of the variations of each

with respect to crystallographic directions and preferred planes containing specific bonding characteristics (as revealed quantitatively from phonon force constants for each atomic pair, and qualitatively from charge density difference contours). Comparisons of the predicted quantities with available experimental data revealed reasonable agreement up to 500 K. Computed properties were interpreted in terms of the cellulose I_β structure and bonding interactions.

Keywords: crystalline cellulose, first-principles density functional theory, thermodynamic properties, mechanical properties

(Some figures may appear in colour only in the online journal)

S Online supplementary data available from stacks.iop.org/MSMSE/22/085012/mmedia

1. Introduction

Cellulose is the most abundant and ubiquitous organic substance on earth. It is the basis of numerous products of critical importance to society, including the paper on which the articles we read are printed, cellophane and textiles that can be renewably produced [1–3], home insulation [4], adhesives [5] and cellulose fiber-reinforced composites, such as thermoplastic composites for automotive structural applications [6–8] and cement composites [9]. The advent of cellulose nanomaterials (CNs), of which cellulose is the main building block, has stimulated new research aimed at understanding the structure and properties of these materials and how to exploit their unique properties in new technologies [10–12]. CNs have a unique combination of characteristics (e.g. high aspect ratio, high mechanical properties, low coefficient of thermal expansion, high thermal conductivity, etc) that differentiate them from other polymers. The vast potential for CNs makes them attractive for a wide variety of applications which include multifunctional films, flexible displays, composite materials, biomedical implants, pharmaceuticals, drug delivery, fibers and textiles, batteries and supercapacitors, electroactive polymers, and many others [10, 13]. Another specific example is the integration of inorganic electronic devices onto polymer substrates (e.g. flexible transparent electronics), in which additions of CNs help to minimize differences in mechanical and thermal properties between the polymer substrate and the inorganic materials making up the device. For the development of new polymer nanocomposite systems there is a greater reliance of composite design models that required reliable material properties. The properties of CNs strongly depend on the properties of crystalline cellulose, e.g. its volume fraction and its distribution within CNs. Of particular importance are the mechanical and thermodynamic properties of crystalline cellulose [10, 11] which have received only minimal attention in scientific and engineering literature. The design of new CN-based materials, and ultimately their ability to meet a wide variety of in-service conditions will be critically dependent upon how cellulose properties vary with temperature [14].

Cellulose is a polysaccharide consisting of linear molecular chains with a repeat unit comprised of two anhydroglucose rings ($(C_6H_{10}O_5)_n$; $n = 10\,000$ to $15\,000$) connected through glycosidic oxygen bridges (i.e. β 1–4 glucosidic bond) [11]. It is produced by trees, plants, algae, bacteria, and it is found in the dermis of certain marine creatures (e.g. tunicates [15]). During biosynthesis, multiple cellulose chains form bundles, called cellulose fibrils, which have regions where the cellulose chains arrange with a high degree of order, resulting in crystalline-like behavior, and regions that are disordered and hence amorphous-like. Naturally occurring cellulose crystals co-exist in two polymorphs, I_α and I_β, with the latter

being the more thermodynamically stable phase [10, 16, 17] and the focus of this study. Cellulose I_β has a monoclinic $P2_1$ (#4) structure [18] (see figure 1). Its crystal structure (e.g. cellulose chain structure and cellulose chain arrangement) and the bonding associated with the linear molecular chains result in extreme anisotropy of its mechanical and thermodynamic properties. These properties, which include the elasticity tensor, thermal expansion coefficients (TECs), isobaric heat capacity, and thermal conductivity, are either incompletely understood or simply have not been measured reliably for the crystalline cellulose I_β structure. Difficulties in experimental testing, propagation of uncertainties in experimental tests [19], and intrinsic material variability in crystalline cellulose test specimens (e.g. different crystal structures, defects, percent crystallinity, etc) render such measurements very challenging [10].

Since the CN structure is anisotropic, it is necessary to understand how the properties change as a function of orientation. However, quantitative characterization of CNs remains elusive, and what is available is incomplete. To fill in these gaps, there has recently been a greater emphasis on predictive modeling of CN properties and property anisotropy. Recent theoretical efforts aimed at predicting cellulose properties have shown substantial differences in certain properties, such as Young's modulus, which are likely due to differences in model parameters, simulation method, configuration of the modeled structure, and whether or not hydrogen bonding [17] and van der Waals (vdW) interactions are incorporated [10, 20]. Alternatively, experimental values of Young's modulus have been determined using different experimental techniques. For instance, x-ray diffraction measurements [21–25] of the axial elastic modulus, measured along the longitudinal axis of the cellulose I_β unit cell (i.e. the a axis denoted in figure 1), range from 90 to 138 GPa. Recently, Diddens *et al* [26] reported an axial elastic modulus of 220 ± 50 GPa and transverse elastic modulus, measured in a direction perpendicular to the longitudinal axis cellulose I_β unit cell, of 15 ± 1 GPa using inelastic x-ray scattering (IXR). More recently, Lahiji *et al* [27] and Wagner *et al* [19] measured a transverse elastic modulus of 8.1 GPa through nanoindentation using atomic force microscopy (AFM). When measurement uncertainties in AFM are accounted for, nanoindentation results in a more broad 2.7–20 GPa range [19].

Similarly, data from experimental measurements for linear TECs (ξ_i) of cellulose I_β also contain considerable scatter [28–31]. For example, the range of reported ξ_i values along the a, b and c axes of the I_β structure (see figure 1) are, respectively, $\xi_1 = (9.8 - 13.6) \times 10^{-5}\,\mathrm{K}^{-1}$ [29, 31], $\xi_2 = (0.5 - 2.1) \times 10^{-5}\,\mathrm{K}^{-1}$ [29, 30] and $\xi_3 = 0.6 \times 10^{-5}\,\mathrm{K}^{-1}$ [29]. An additional challenge for experimental measurements stems from the I_β structure transition to a high-temperature phase at temperatures approaching 475–500 K: this high-temperature cellulose phase has mechanical and thermal properties that considerably differ from the $P2_1$ structure [31]. To the best of our knowledge, numerical predictions of ξ_i values for crystalline cellulose I_β in the extant literature have only been obtained with molecular dynamics using various force fields (GROMOS 45a4 [32], GLYCAM06 [9], GROMOS 53a6 [33] and ReaxFF [34]) reporting, respectively, values of $\xi_1 = 7.3 \times 10^{-5}$–$10.8 \times 10^{-5}\,\mathrm{K}^{-1}$, $\xi_2 = 0.91 \times 10^{-5}$–$2.9 \times 10^{-5}\,\mathrm{K}^{-1}$ and $\xi_3 = -3.0 \times 10^{-5}$–$2.9 \times 10^{-5}\,\mathrm{K}^{-1}$ in the 280–400 K range. Existing experimental and theoretical studies suggest a relatively high axial elastic modulus and low axial thermal expansion of cellulose I_β compared to other organic compounds, such as polymers, which have elastic moduli in the 10^{-2}–10^{1} GPa range, and linear thermal expansion values within $(5–20) \times 10^{-5}\,\mathrm{K}^{-1}$. Additionally, the large difference between transverse and axial elastic moduli, as well as differences between the ξ_i for cellulose I_β indicate extreme property anisotropies that result from its bonding interactions. Hatakeyama *et al* [35, 36] measured C_p for amorphous cellulose using differential scanning calorimetry (DSC) and extrapolated their values to crystalline cellulose obtaining $C_p = 202.7\,\mathrm{J\,mol\text{-}f.u.}^{-1}\,\mathrm{K}^{-1}$ (at 360 K) and $C_p = 218.9\,\mathrm{J\,mol\text{-}f.u.}^{-1}\,\mathrm{K}^{-1}$ (at 420 K).

First-principles density functional theory (DFT) within the quasi-harmonic approach has previously been used to predict elasticity tensor components, anisotropy of Young's moduli and Poisson's ratio, the ξ_i and the isobaric heat capacity, C_p, for numerous materials with reasonable accuracy relative to existing experimental results [37–39]. However, a careful search of the literature revealed a dearth of theoretical predictions of these important properties for crystalline cellulose. This situation is no different for thermal conductivity (λ) values for cellulose I_β. Most of the existing literature on thermal conductivity measurement of cellulose focuses on cellulose nanofibrils (CNFs) which are finer cellulose fibrils produced from wood and plant fibers, each containing ~100% cellulose in both amorphous and crystalline forms. For example, Shimazaki *et al* [40] produced 70 μm thick CNFs (58 wt%)-epoxy matrix reinforced composite films that had a measured thermal conductivity of 1.1 $W\,m^{-1}\,K^{-1}$ along the film in-plane direction and 0.23 $W\,m^{-1}\,K^{-1}$ along the thickness direction. These values were measured at room temperature using alternating current (ac) calorimetry [41] and thermal wave analysis [42]. Results showed that there is a 7–8 times increase in the thermal conductivity along the in-plane direction of the film and a 1–2 times increase along the thickness direction compared to the neat epoxy matrix. The increased thermal conductivity of the composites suggests that they have the ability to dissipate more heat for a given input heat flux, which lowers the composite temperature and thus improves the thermal stability, preventing chemical and mechanical degradation [10]. Recent predictions of thermal conductivity of simple oxides using DFT have produced results that differ by 15–40% from experimental values [43–45]. As shown by Chen and Podlucky [46], calculation of the electronic thermal conductivity from DFT is challenging since existing techniques that have been discussed in the literature are unreliable for insulating materials.

Our previous study of the cellulose I_β structure focused on predicting the anisotropy of Young's moduli and Poisson's ratio using first-principles DFT with vdW interactions [47]. All computed results were relevant for 0 K (without zero-point energy (ZPE) corrections from vibrational calculations) as no attempt was made to explore temperature variations of any property. In the present study, however, we employ DFT with vdW corrections [48] to compute vibrational properties from phonon calculations, finite temperature thermodynamic properties (entropy S, enthalpy H and C_p via the quasi-harmonic approach) [37, 49–51], linear TECs, ξ_i, and stiffness matrix components, C_{ij}, of the cellulose I_β structure. The temperature dependences of ξ_i and C_{ij} are predicted using the quasi-harmonic approach whose main inputs are the predicted strain/elasticity–volume–temperature relationships [39, 52]. Temperature variations of the Young's modulus and Poisson's ratio with respect to crystallographic orientation are computed based on the stiffness matrix, C_{ij}. Reverse, non-equilibrium molecular dynamics (RNEMD) simulations are used to compute the thermal conductivity tensor of monoclinic cellulose I_β. Inherent computational challenges with DFT, mainly due to the CPU time limitations, and its inability to properly describe the details of weak interactions between molecules that determine the thermal properties for slow processes, such as thermal conduction, make the RNEMD method using an empirical force field attractive for the present calculations [53]. Calculated cellulose I_β properties are compared with available experimental data in the literature and interpreted in terms of cellulose I_β bonding mechanisms.

2. Background

The present study focuses on the $P2_1$ (#4) cellulose I_β structure as experimentally determined by Nishiyama *et al* [18] using x-ray and neutron fiber diffraction: $a = 7.784$ Å, $b = 8.201$ Å,

$c = 10.380$ Å, $\alpha = 90^\circ$, $\beta = 90^\circ$ and $\gamma = 96.55^\circ$ [18]. The cellulose I_β primitive cell consists of two $C_6H_{10}O_5$ units, while the crystallographic (conventional) cell contains four $C_6H_{10}O_5$ units. Cellulose I_β also contains intra- and inter-chain hydrogen bond network patterns. Nishiyama *et al* [18] described the two networks with different relative occupancies according to the cellulose I_β polymorph: network A and network B. Network A occupies ~70–80% of all the chain positions in I_β, and only ~55% in I_α [54, 55]. The present study focuses on cellulose I_β with network A since it is the most commonly occurring cellulose polymorph in higher plant cell walls and in tunicates [56]. Two views of this crystalline structure of cellulose I_β are shown in figure 1. Figure 1(*a*) shows the projection along the *b* axis direction and figure 1(*b*) shows the projection along the *a* axis direction. Figure 1(*b*) depicts the cellulose chains along the hydrogen bonded planes (in the *b*–*c* plane). These planes are stacked one above the other as shown in figure 1(*a*). The interaction between planes is mainly governed by weak vdW interactions and, to a lesser degree, by some intermolecular hydrogen bonds [58]. Within the *b*–*c* plane, the bonding along the *c*-axis direction is stronger than that along the *b*-axis direction mainly due to covalent bonding. The crystallographic directions and the *a*, *b* and *c* axes are also included in the figure. To facilitate our predictions of the anisotropy of Young's modulus and Poisson's ratio of monoclinic cellulose I_β, we define a Cartesian system of coordinates with axes 1, 2 and 3. Direction 1 is chosen to be parallel to *a* [57], and direction 3 is parallel to *c* ([0 0 1]). For the monoclinic $P2_1$ structure, *b* is not orthogonal to *a*. Therefore, direction 2 is chosen such that it is orthogonal to directions 1 and 3.

3. Computational methodologies

3.1. DFT and phonon calculations

All DFT calculations in the present study were performed with the VASP 5.2.12 code [59, 60]. The Kohn–Sham equations were solved with a plane-wave basis set using the projector augmented wave (PAW) method [61] and the exchange-correlation energy was described by the generalized gradient approximation of Perdew–Burke–Ernzerhof (GGA-PBE) [62]. For C, four electrons ($2s^2 2p^2$) are treated as valence, one for H ($1s^1$) and six for O ($2s^2 2p^4$). Standard density functionals based upon the LDA (local density approximation) and GGA do not account for the vdW interactions. To solve this problem, Grimme [48] proposed a semi-empirical correction for vdW interactions, renamed as PBE-D2 [63]. This scheme was employed by Dri *et al* [47] to compute the C_{ij} and S_{ij} of crystalline cellulose at 0 K and is adopted for the current study as well.

Three successive full-cell optimizations, involving simultaneous minimization of all Hellman–Feynman force and stress tensor components via a conjugate gradient method, were conducted (adapting basis vectors and computational grids to the cell parameters) to ensure convergence of cell energies and structural parameters. The total energy was converged to 10^{-7} eV and the force components were relaxed to at least 10^{-4} eV Å^{-1}. For all calculations (i.e. structural and elastic properties), a $7 \times 7 \times 7$ *k*-point mesh, corresponding to a *k*-point spacing of $0.110 \times 0.086 \times 0.110$ Å^{-1}, was used.

Phonon calculations were based upon the supercell method. The longitudinal and transverse optical (LO–TO) zone center splittings for the infrared active modes in cellulose I_β were ignored since these have a negligible effect on the computed thermodynamic properties [49, 50]. Force constants, i.e. the Hessian matrix, were calculated in real space using a cellulose I_β $2 \times 1 \times 2$ supercell containing 336 atoms. The large number of symmetry-unique atomic sites required 252 VASP single point energy calculations. Atomic displacements of ± 0.02 Å were

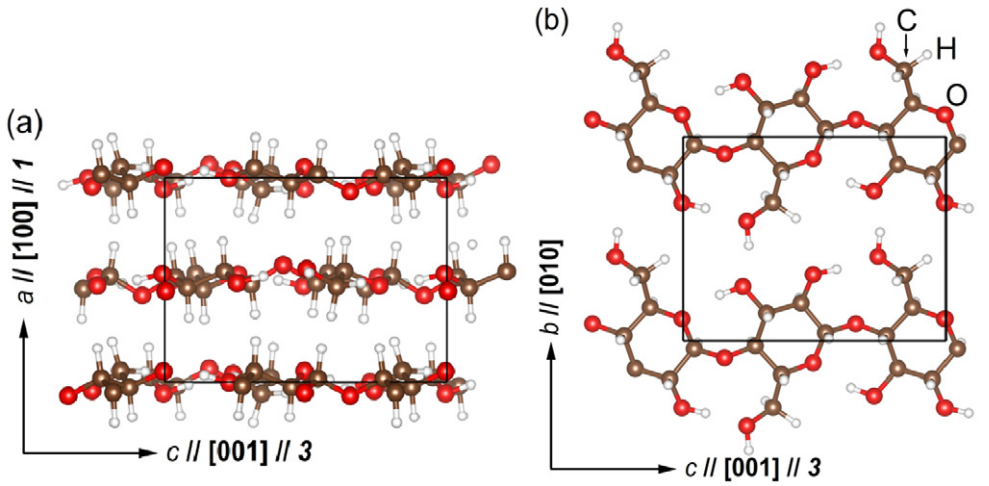

Figure 1. Projected structure of cellulose I_β (space group $P2_1$) along the b axis direction (a) and along a axis direction (b), showing an obvious layered structure of I_β along the a axis direction, and weaker bonding along the b axis direction with respect to that of c axis direction. Red spheres denote oxygen ions, brown spheres represent carbon ions and white spheres represent hydrogen ions. The solid lines connecting spheres represent covalent bonds. For simplicity, non-bonding interactions are not denoted in either figure. The rectangles in (a) and (b) show the conventional I_β cell. The structure and lattice parameters are those determined experimentally by Nishiyama *et al* [18] using x-ray and neutron fiber diffraction.

employed for the independent atoms and a $2 \times 1 \times 2$ k-point mesh ($0.279 \times 0.201 \times 0.259$ Å^{-1}) was used for each single point energy calculation.

Additional details on our computational methodologies are in appendix A.

3.2. Finite temperature calculations

3.2.1. Thermodynamics. The quasi-harmonic approach was used to calculate first-principles thermodynamics quantities at finite temperatures. This required evaluation of the Helmholtz energy, $F(V, T)$, at volume V and temperature T, given by [37, 49–51]

$$F(V, T) = E(V) + F_{\text{el}}(V, T) + F_{\text{vib}}(V, T). \tag{1}$$

Here, $F_{\text{el}}(V, T)$ represents the thermal electronic contribution evaluated from the electronic density of states (DOS). This term, which is important for metals with non-zero electronic DOS at the Fermi level, is ignored since cellulose I_β is an insulator. The vibrational contribution to $F(V, T)$, which was obtained from the total phonon DOS at six volumes in the present study, is $F_{\text{vib}}(V, T)$. Note that F_{vib} at 0 K contains a zero-point vibrational energy (ZPE) contribution due to quantum fluctuations at the ground state, which can be estimated from the phonon DOS [72]. The static energy at 0 K without the ZPE in equation (1) is $E(V)$: this term was determined by fitting the first-principles energy versus volume (E–V) data points according to a four-parameter Birch–Murnaghan equation of state (EOS) [37]

$$E(V) = k_1 + k_2 \times V^{-2/3} + k_3 \times V^{-4/3} + k_4 \times V^{-2}, \tag{2}$$

where k_1, k_2, k_3 and k_4 are fitting parameters (the pressure–volume version of equation (2) is listed in the footnotes to table 1). The equilibrium properties estimated from this EOS include

Table 1. Structural parameters (lattice parameters a, b, c, cell angle γ, and equilibrium volume, V_0), and elastic moduli (the bulk modulus B_0 and its pressure directive B_0') computed with DFT/phonon compared with available experimental data. Additional results at higher temperatures are shown in figure 5 and in table S3 of the online supplementary material (stacks.iop.org/MSMSE/22/085012/mmedia).

Method	a (Å)	b (Å)	c (Å)	γ (°)	V_0 (Å^3)	B_0 (GPa)	B_0'
PBE-D2, this work, 0 K[a]	7.618	8.139	10.399	96.59	640.57	16.1	6.69
PBE-D2, this work, 0 K[b]						17.4	7.46
PBE-D2, this work, 0 K[c]	7.752	8.153	10.409	96.40	653.80	13.9	
PBE-D2, this work, 295 K[c]	7.896	8.167	10.418	96.12	667.92	10.0	
PBE-D2, other work, 0 K	7.57[d]	8.14[d]	10.39[d]	96.5[d]	636[d]	16[e]	
PBE-D2, other work, 0 K[f]	7.85	8.18	10.47	96.5	668		
PBE-D2, other work, 0 K[g]	7.56	8.13	10.39	96.7	635		
Expt., 15 K[h]	7.64	8.18	10.37	96.54	643.9		
Expt., room temperature	7.76[h]	8.20[h]	10.37[h]	96.62[h]	655.5[h]	19.8 ± 2.9[i]	27.6 ± 6.2[i]
Expt., room temperature[j]	7.82	8.26	10.40	96.3			

[a] Calculated results without ZPE based on the energy–volume EOS, i.e. equation (2).
[b] Calculated results without ZPE based on the pressure–volume EOS $P(V) = -\partial E/\partial V = 2k_2/3V^{5/3} + 4k_3/3V^{7/3} + 2k_4/V^3$.
[c] Calculated with ZPE based on the quasi-harmonic approach, see equation (1).
[d] Calculated without ZPE [16].
[e] Fit using DFT-computed data points and Murnaghan's EOS [63].
[f] Calculated by ESPRESSO using norm-conserving pseudopotentials [77].
[g] Calculated using simultaneous optimization of the lattice parameters and ionic degrees of freedom [47].
[h] Measured by neutron diffraction at 295 K [55].
[i] Fit of the Birch–Murnaghan EOS to the measured pressure–volume data points at 15 K (there is noticeable scatter in these data points [2]).
[j] Measured by x-ray [2].

the volume, V_0, the electronic energy, E_0, the bulk modulus, B_0, and the bulk modulus pressure derivative, B_0'. In the present study, the quasi-harmonic method in equation (1) was used to compute entropy, S, enthalpy, H, the isobaric heat capacity, C_p, the equilibrium volume as a function of temperature, $V_0(T)$, and the (average) linear TEC (ξ), (see detailed methodologies in [24, 35]). The C_p was computed from

$$C_p(T) = C_V(T) + \alpha_V^2(V,T)T\,B(T)V_0T, \tag{3}$$

where $C_V(T)$ is the constant volume (or isochoric) heat capacity (from the phonon calculations), T temperature, $B(T)$ the isothermal bulk modulus and α_V the volume thermal expansion.

3.2.2. Elastic moduli and thermal expansion. Cellulose I_β, like many other single crystals, exhibits anisotropic properties under loading with respect to an intrinsic direction in the material. As such, its elastic mechanical behavior under an infinitesimal applied strain is described as $\sigma_{ij} = C_{ijkl}\varepsilon_{kl}$ (Einstein notation) whereas σ_{ij} and ε_{kl} represent, respectively, the second-order stress and strain tensors. The fourth-order stiffness tensor is C_{ijkl}. The inverse relation can also be written as $\varepsilon_{ij} = S_{ijkl}\sigma_{kl}$, where S_{ijkl} are the components of the elastic compliance tensor. Considering the monoclinic structure of cellulose I_β, with its symmetry plane defined by the c axis (see figure 1), the stiffness and compliance tensors can be expressed as matrices by C_{ij} and S_{ij}, respectively, each with 13 independent quantities [73]. Figure 2 shows a schematic representation of the cellulose I_β unit cell, the Cartesian coordinate system

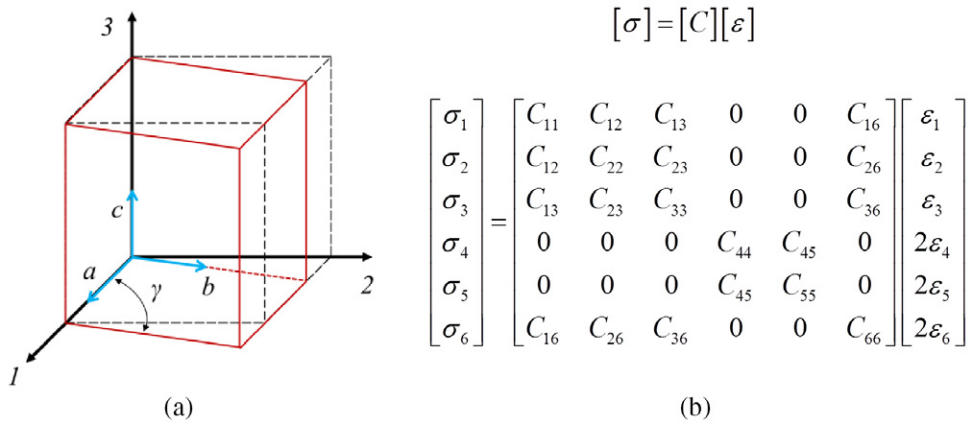

Figure 2. (*a*) A schematic representation of the cellulose I_β monoclinic unit cell (red solid lines), together with a Cartesian coordinate system (black solid lines) and a cubic cell (black dashed lines). This highlights the non-orthogonal relation between a and b. (*b*) The relationship between the stiffness matrix, C_{ij}, connecting stresses, σ_i, and strains, ε_i, in the monoclinic unit cell is also shown [74].

used as the frame of reference in this study and the monoclinic stiffness matrix associated with it. Using the computed C_{ij} at different temperatures, and knowing the crystallographic orientation of the cellulose unit cell with respect to a global coordinate system (see figure 2), it is possible to compute the temperature variation of Young's modulus. This is defined as the slope between the normal stress and the longitudinal strain under simple tension along a specific crystallographic direction. Similarly, Poisson's ratio is defined as the ratio of the lateral strain to the longitudinal strain in simple tension. Once Poisson's ratio is computed for a sufficient number of directions, a 3D representation can be constructed to display its variation with crystallographic direction. All orientations are unequivocally defined by the Miller indices in conjunction with the reference Cartesian coordinate system shown in figure 2. The methodology we used to compute the elastic moduli (i.e. Young's modulus and Poisson's ratio) was previously applied to compute the elastic moduli of crystalline cellulose at 0 K by Dri *et al* [47].

Similarly, the six independent linear TECs, ξ_i, can be derived as a function of temperature at constant pressure, P, via

$$\xi_i = \left(\frac{\partial \varepsilon_i(T)}{\partial T}\right)_P. \tag{4}$$

The same Cartesian coordinate system relative to the original cellulose I_β crystalline structure as depicted in figure 2 can be used. As such, the strains as a function of volume, $\varepsilon_i(V)$ can be calculated with DFT at 0 K using the relaxed lattice vectors at different volumes. The volume–temperature relation, $V(T)$, or inversely $T(V)$, can be predicted with the quasi-harmonic approach given in equation (1). Once these relationships are obtained, the temperature-dependent ξ_i can be expressed as functional of V, namely, $\xi_i(T) = \xi_i\,(T(V))$. This is obtained by employing a quasi-static approach (specifically for temperature-dependent properties) without considering the kinetic energy and the fluctuation of microscopic stress tensors at high temperatures. For this purpose, the quasi-static approach combines $\varepsilon_i(V)$ and $T(V)$ following the procedure detailed in [39, 52].

The $C_{ij}(T)$ can be calculated using the values of C_{ij} for different volumes and the $T(V)$ relation as mentioned above, namely, $C_{ij}(T) = C_{ij}(T(V))$ [39, 52]. Note that the measured C_{ij} at high temperatures (e.g. using the resonance method) is usually isentropic since the system is adiabatic due to the faster speed of elastic waves relative to heat diffusion [39]. The thermodynamic relations between the isothermal and isentropic elasticity matrices were given by Davies [75] and others [39].

3.3. Thermal conductivity

The thermal conductivity, λ, is the proportionality constant that relates the heat flux, j, to the driving force of a temperature difference, $\mathrm{d}T/\mathrm{d}z$:

$$j_z = -\lambda \frac{\mathrm{d}T}{\mathrm{d}z}, \tag{5}$$

where the z direction is arbitrarily taken for convenience. The simplest way to implement this in a molecular dynamics code is to compute the temperature profile across a slab of the material by coupling one side to a cold temperature bath and the other to a hot one, and computing j. This, however, creates issues with the conservation of energy in the system since it is coupled to two heat baths which are adding and removing energy. As such, the calculations become very sensitive to the way the coupling to the heat baths is modeled.

Müller-Plathe [76] realized that there was an elegant solution to this issue: rather than drive the temperature of the system as one would do in a physical system, in the computational experiment one can produce a heat flux by exchanging the momenta of particles in the cold region with those in the hot region, and then measure the resulting temperature profile. This is the RNEMD approach to transport, which neatly circumvents the issues of conservation of energy. In practice, the simulation is performed on a sample of material elongated in the z direction (for example), which is conceptually divided into a number of layers—typically about 30—in that direction. Every so often, the momentum of the hottest particle in the cold layer is swapped with that of the coldest particle in the hot layer. This has the effect of producing a heat flux, which is measured from the cold layer to the hot layer. In response, the system develops a temperature gradient between the hot and cold layers, which can be measured through the average temperature in each of the layers between the hot and cold layers. The rate of momentum transfer is adjusted to provide a reasonable ramp in the temperature. If the system is driven too hard, then the temperature profile will not be linear. However, if the system is driven too gently, then the natural fluctuations of the temperature in a small sample will reduce the accuracy of the measured temperature ramp.

4. Results and discussion

4.1. Cellulose I_β bonding

Figure 3 shows the original crystalline structure (as shown in figure 1) with the isosurfaces of charge gains (yellow contours in $\Delta\rho/\text{Å}^3$) calculated with PBE-D2. These results are indicative of the charge density redistribution upon formation of the cellulose I_β structure. They were computed from the difference between the charge density after electronic relaxations and the reference or non-interacting charge densities from C, O and H calculated from one electronic step (see equation (14) in [56]).

Phonon calculations allow quantitative analysis of the interactions between atomic pairs using force constants [66]. Force constants quantify the extent of interaction between atoms.

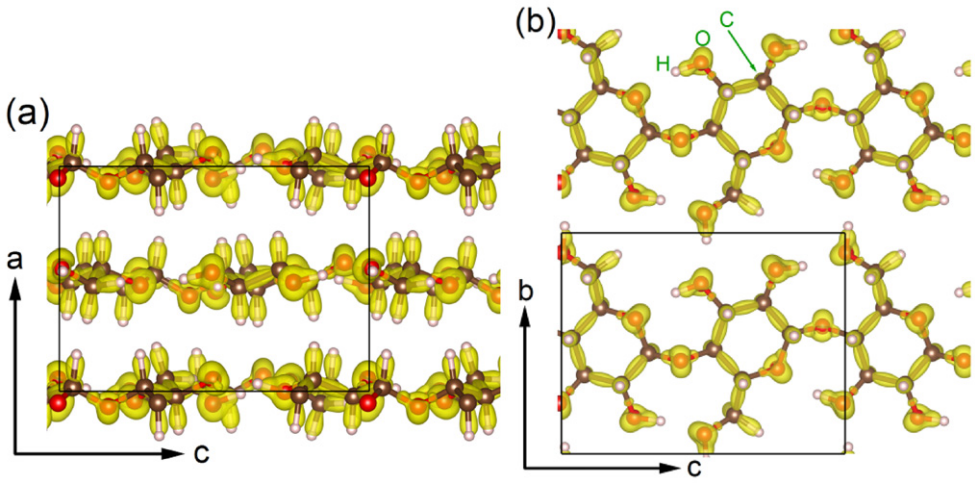

Figure 3. Projected structures and charge gains of cellulose I_β with space group $P2_1$ along the b axis direction (a) and along the a axis direction (b), showing the layered structure of I_β along a axis direction, and weaker bonding along the b axis direction with respect to that of the c axis direction in terms of the density of charge gains. Red spheres denote oxygen ions, brown spheres represent carbon ions and white spheres represent hydrogen ions. The charge gains calculated with PBE-D2 are also shown, illustrated in the change density difference ($\Delta\rho/\text{Å}^3$, the yellow colors) isosurfaces, where the reference density is the reference charge density calculated in one electronic step.

Figure 4 shows the key stretching force constants (>0.1 eV Å^{-2}) of cellulose I_β at its theoretical equilibrium volume at 0 K (see table 1).

As expected, the O–H atomic pairs are predicted to have the strongest interaction (∼36 eV Å^{-2}) with the smallest bond lengths (∼1 Å), followed by C–H atomic pairs (∼27 eV Å^{-2} with bond lengths ∼1.1 Å), C–O pairs (∼20 eV Å^{-2} with bond lengths ∼1.4 Å), and the C–C pairs (∼15 eV Å^{-2} with bond lengths ∼1.5 Å), and H–H pairs (∼1.7 eV Å^{-2} with bond lengths ∼1.8 Å) see also the online supplemental table S2 (stacks.iop.org/MSMSE/22/085012/mmedia). The strong O–H and C–H interactions are indicative of their critical role in stabilizing the cellulose I_β structure. The strong interactions between the O–H, C–H, C–O and C–C atomic pairs are also indicated by the isosurfaces of the charge density difference contours of figure 3. The charge gains in figure 3 are also suggestive of bond directionality between the O–H, C–H, C–O and C–C pairs, hence providing an indication of their covalent character. The data presented in figures 3 and 4 supports the fact that interaction in the cellulose I_β structure is strongest along the c axis, and it is weakest along the a axis. Predicted values of C_{ij} and ξ_i (discussed below) further confirm these observations.

4.2. Structural properties

Table 1 summarizes the predicted structural properties for cellulose I_β based on the PBE-D2 method, including the lattice parameters and cell angle γ for the conventional cell, and the equilibrium properties V_0, B_0 and B_0' estimated using the EOS in equation (2). Our computed structural properties are in reasonable accord with experimental data at 15 and 295 K [2, 55] and other PBE-D2 predictions [16, 63, 77]. For example, our computational approach based upon electronic energies alone predicts the value of a to be 1.72% lower than the true 0 K

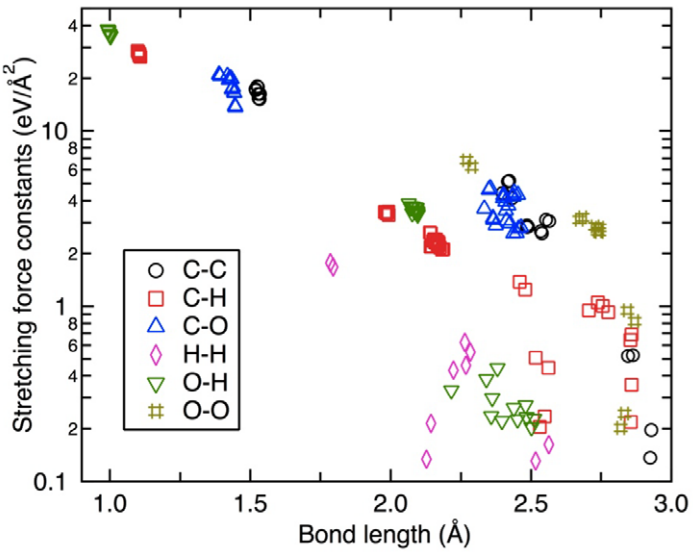

Figure 4. Key stretching force constant variation (from phonon calculations) with bond length for each ionic pair in the cellulose I_β structure (see also table S2 in the online supplementary material (stacks.iop.org/MSMSE/22/085012/mmedia) for specific numerical values). The ordinate is on a log scale. A large positive force constant suggests strong interaction, while the small values (<0.1 eV Å^{-2}) are ignored in this plot.

value with the ZPE correction, and only 0.28% lower than the measured value at 15 K [55]. For b, our values are 0.17% lower than the 0 K with the ZPE correction, and 0.50% lower than the measured ones at 15 K. Finally, for c our values are 0.009% lower than the 0 K with the ZPE correction, and 0.28% lower than the measured ones at 15 K. The prediction for γ is even better, yielding only 0.05% with respect to the experimental value at 15 K (see table 1 for additional comparisons).

We note V_0, B_0 and B_0' provide a useful means for (i) validating DFT calculations against available experimental data; (ii) calculating the EOS (equation (2)) used in the quasi-harmonic approach (equation (1)); and (iii) providing a qualitative estimate of the thermal expansion (B_0' is related directly to the Grüneisen constant, from which the thermal expansion can be estimated via the Debye model, for example [37, 66]). In addition, the larger the value of B_0', the larger the value of ξ_i. As for B_0, the present 0 K prediction of 16.1 GPa (using the E–V EOS of equation (2)) or 17.4 GPa (using the P–V EOS derived from equation (2)), is in good agreement with a previous PBE-D2 prediction (16 GPa) at 0 K [63] and the measured data at 298 K (19.8 ± 2.9 GPa) [2]. Concerning B_0', the present study gives a reasonable value of 6.69 (based on the E–V EOS of equation (2)) or 7.46 (based on the P–V EOS derived from equation (2)); however, we believe that the measured B_0' value is too large (27.6 ± 6.2), possibly due to excessive scatter in the reported P–V data points [2], compared with values around 3–6 measured for most materials (i.e. insulators and metals) [78].

4.3. Thermodynamic properties

Figure 5 illustrates the predicted thermodynamic properties (solid curves) of cellulose I_β up to 500 K under external pressure $P = 0$ GPa using the quasi-harmonic approach of equation (1), including H, S and C_p at constant pressure (see equation (3)). Here, the enthalpy is

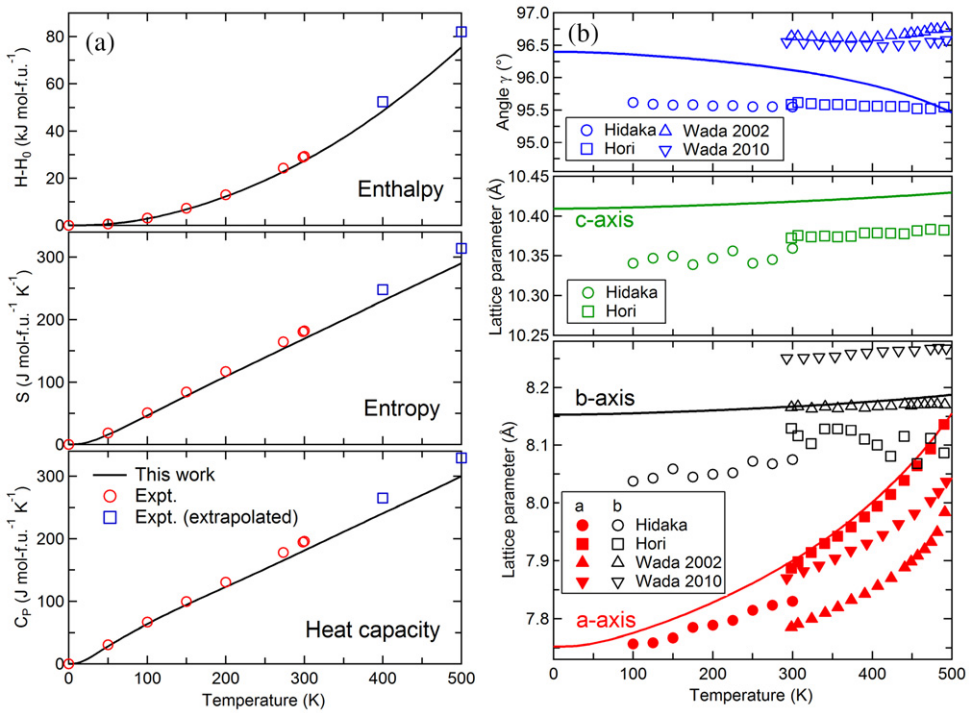

Figure 5. (*a*) Temperature variations for enthalpy, $H - H_0$, entropy S, and isobaric heat capacity, C_p for cellulose I_β from the present calculations (solid curves) and available experimental data (open symbols). Note that (i) H at 0 K, H_0, is the reference state of H [81] and (ii) the experimental data are measured using cotton microcrystalline cellulose with a 90% degree of crystallinity [80] (see also the online supplemental table S1 (stacks.iop.org/MSMSE/22/085012/mmedia) for more details and comparisons between theoretical predictions from the present study and available experimental data). (*b*) Predicted lattice parameters a, b, c, angle γ of cellulose I_β compared with experimental data (open and filled symbols) measured by Hidaka *et al* using wood cellulose [28]; Hori using wood cellulose [29]; Wada using tunicate (halocynthia) [30]; and Wada *et al* using green algae [31]. Calculated values at selected temperatures are also shown in the table S3 of the online supplementary material (stacks.iop.org/MSMSE/22/085012/mmedia).

set to zero at 0 K with the reference enthalpy $H_0 = 445$ kJ/mol-f.u., which is the value of the ZPE at the equilibrium volume at 0 K (653.80 Å^3 per unit cell, see table 1); and each figure is terminated at 500 K which is close to the phase transition temperature of I_β to a high-temperature phase (for which no space group could be located) [30, 31]. Additionally, cellulose exhibits a high thermal decomposition temperature at 593 K [31]. As an example of the main input for equation (1), the phonon DOS at the theoretical equilibrium volume, V_0, is shown in figure S1 of the online supplementary material (stacks.iop.org/MSMSE/22/085012/mmedia) with a maximum frequency around 100 THz and a large gap in states within 45–88 THz. For comparison, the maximum vibrational frequency of the cellulose I_β phase is 3352 cm^{-1} (100.5 THz) measured with Fourier transform infrared (FTIR) spectroscopy [79]. This is in close accord with the maximum vibrational frequency in figure S1 from our phonon calculations. Figure 5 shows that the present predictions of the temperature variation of H, S

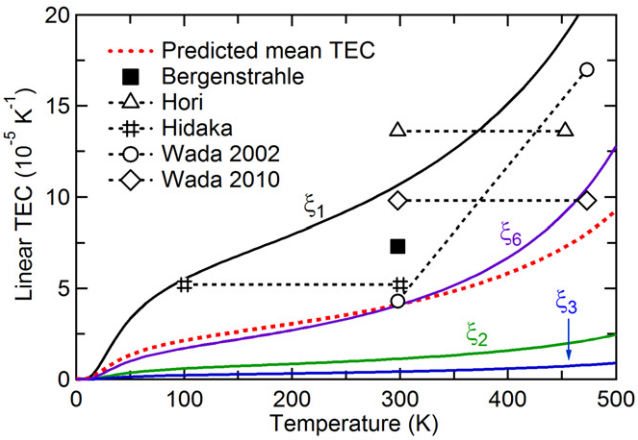

Figure 6. Predicted linear thermal expansion coefficients or TECs ($10^{-5}\,K^{-1}$) and the mean TEC (i.e. average of all components) of cellulose I_β. All solid lines are predictions from the present work. Experimental TECs along the a axis (ξ_1) are shown denoted by symbols with dashed lines. Each corresponds to measurements from the same author(s) (Hidaka *et al* using wood cellulose [28], by Hori using wood cellulose [29], by Wada using tunicate [30], and by Wada *et al* using green alga [31]), at different temperatures. The TEC along the a axis (ξ_1) predicted with molecular dynamics simulation [32] is denoted by the filled square. More details concerning the predicted and calculated TECs are shown in table S4 of the online supplementary material (stacks.iop.org/MSMSE/22/085012/mmedia). Note that ξ_4 and ξ_5 are all zero due to the monoclinic symmetry of the cellulose I_β.

and C_p agree well with available experimental data (open and filled symbols in figure 5(a)) measured using cotton microcrystalline cellulose with a 90% degree of crystallinity, as well as the extrapolated data at high temperatures (>300 K) [80]. Figure 5(a) also indicates that the present predictions are slightly lower than the cotton microcrystalline cellulose measurements, especially at high temperatures (>300 K). Note that the comparisons between the present calculations and the measurements [80] are also given in table S1 of the online supplementary material (stacks.iop.org/MSMSE/22/085012/mmedia) at selected temperatures between 50 and 500 K.

Based on equation (1) and the quasi-static approach described above, the predicted lattice parameters a, b, c, angle γ of cellulose I_β as a function of temperature are shown in figure 5(b). The present predictions agree reasonably well with the scattered data measured by Hidaka and co-workers using wood cellulose [28]; Hori using wood cellulose [29]; Wada using tunicate (halocynthia) [30]; and Wada *et al* using green algae [31]. Calculated values at selected temperatures between 0 and 500 K are also shown in the online supplement table S3 (stacks.iop.org/MSMSE/22/085012/mmedia), including a, b, c, γ and V_0. Clearly, lattice parameter a increases quickly with increasing temperature compared to lattice parameters b and c. This behavior is attributed to the weak interaction along the a axis direction (see figure 1 and the discussion above), which is predominantly governed by vdW forces. As for the cell angle γ, the present work predicts a decreasing trend with increasing T, while the measured values show a (nearly) constant or a slightly increasing trend with increasing T.

Alternatively, the variation of the lattice parameters and angle with respect to T can be used to obtain the linear TECs, ξ_i. Figure 6 shows that the temperature variation of ξ_1 (along

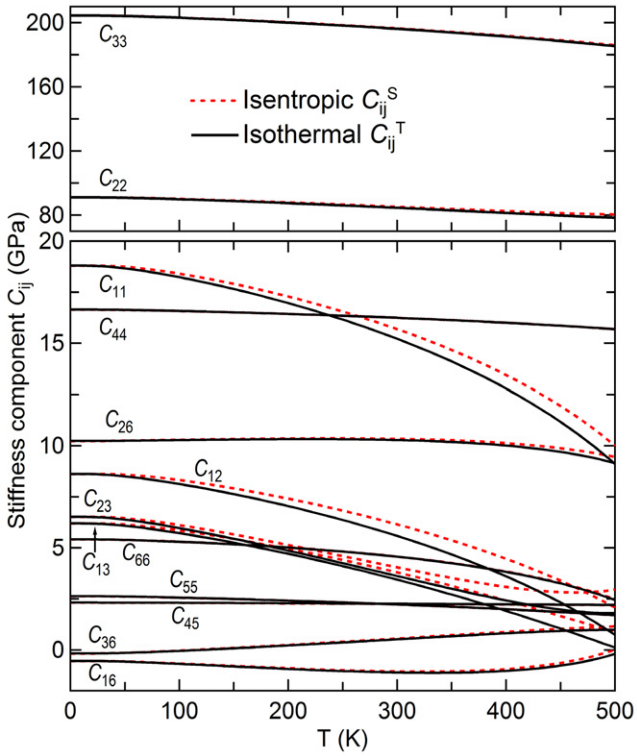

Figure 7. Predicted isothermal and isentropic elastic stiffness matrix components, C_{ij}, of cellulose I_β based on the quasi-static approach.

the a axis direction) agrees reasonably well with the rough estimates from measurements [28–31] and molecular dynamics simulations [32] (open and filled symbols). In addition, ξ_1 is larger than ξ_2 (roughly along the b axis direction) and ξ_3 (along the c axis direction), agreeing with the measurement data [28–31] shown in table S4 of the online supplementary material (stacks.iop.org/MSMSE/22/085012/mmedia). The fact that ξ_1 exceeds ξ_2 and ξ_3 makes sense when one considers the cellulose I_β structure shown in figure 1 and the weak interlayer interaction forces along the 1 direction. Note also that ξ_6 (within the a–b plane, see figure 2) is close to the mean value of all of the TECs, while ξ_4 and ξ_5 are all zero due to the monoclinic symmetry of the cellulose I_β. It is worth mentioning that our predicted TECs (e.g. ξ_1) vary smoothly with temperature, while there is a notable temperature insensitivity suggested by several of the experimental studies (figure 6). However, the other thermodynamic properties predicted in the present study are smaller than corresponding measured values (see figure 5). This suggests the following explanations for the noted discrepancies: (i) uncertainties in the measurements and (ii) possible issues with the chosen exchange-correlation functional in the present study.

4.4. Elastic properties

Figure 7 shows the predicted isothermal and isentropic stiffness matrix components, C_{ij} (up to 500 K) using the quasi-static approach—no experimental data could be located in the literature. Additional details associated with the calculation of the predicted isothermal and isentropic

Table 2. Elastic properties (C_{ij}, B, E and ν) of cellulose I_β at $T = 0$ K (without the ZPE correction from phonon calculations) obtained in this study versus experimental values of E and ν. All moduli (except for ν) are in GPa. Note that Young's modulus as a function of direction is shown in figure 8, and the C_{ij} at high temperatures predicted by the quasi-static approach are shown in figure 7 and table S5 in the online supplementary material (stacks.iop.org/MSMSE/22/085012/mmedia).

C_{ij} (GPa) (this study)						$\boldsymbol{B}$ (GPa)	$\boldsymbol{E}$ (GPa)	ν
22.1	11.5	9.2	0	0	0.7	19.8 ± 2.9[a]	145, 150[b]	0.377[h]
	98.9	10.3	0	0	9.7		120–135	0.639[h]
		213.3	0	0	−1.1		134[d], 143[e]	0.442[h]
			17.1	2.4	0		15, 220[f]	
				3.1	0		2.7–20[g]	
					5.9			

[a] Fitted using the Birch–Murnaghan EOS based on the measured pressure–volume data points, but these data points are scattered [2].
[b] Axial elastic modulus measured by AFM using tunicate microfibrils [82].
[c] Axial elastic modulus measured by x-ray measured in the c direction at 300 K using microfibers [23].
[d] Axial elastic modulus measured by x-ray measured in the c direction at 300 K using microfibers [21].
[e] Axial elastic modulus measured by Raman spectroscopy using tunicate whiskers [83].
[f] Elastic modulus measured by IXR with 15 GPa (transverse) and 220 GPa (axial) [26].
[g] Transverse elastic modulus using AFM nanoindentation [19, 27].
[h] Measured by x-ray on ramie for tension along [0 0 4] and negative strain along [2 0 0], i.e. 0.377 for [2 0 0]/[0 0 4], 0.639 for [1 1 0]/[0 0 4] and 0.442 for $[1\ \bar{1}\ 0]$/[0 0 4] [84].

stiffness matrix components are found in Appendix B. The temperature-dependent elastic stiffness matrix components along with the bulk modulus (B), shear modulus (G), Young's modulus (E) and Poisson's ratio (ν) are listed in table S5 of the online supplementary material (stacks.iop.org/MSMSE/22/085012/mmedia) at selected temperatures between 0 and 500 K. The fact that the isentropic C_{ij} values are greater than (or equal to) the isothermal values can be attributed to the positive (or zero) TECs (see figure 7) [39, 75]. Most of the C_{ij} values are predicted to decrease with increasing T, as expected. In addition, C_{11} decreases rapidly with increasing temperature change. As such, C_{11} is the most sensitive to temperature increases, followed by C_{12}, C_{13} and C_{23}. We surmise that this is mainly caused by the extremely large variation of ξ_1 along the a axis direction (see figures 1(a) and 6). This trend is not observed for C_{16} and C_{36}, which denote more complex elastic deformations: each is close to zero for the temperature range considered in figure 7. The minimum value of C_{16} occurs around 350 K. These results suggest only a minimal connection between the stress along the a axis direction and the transverse shear stress.

Table 2 summarizes the predicted elastic properties, namely, C_{ij}, B, E, and v of cellulose I_β under the theoretical equilibrium volume, $T = 0$ K, without the ZPE correction from phonon calculations. Our calculations suggest that $C_{33} = 213$ GPa is the largest of the elastic stiffness matrix components (similar to the results obtained by Dri *et al* [47]). This is comparable to the C_{ij} of the 3d transition metals Fe, Ni, Cu, etc [85, 86]. However, the other C_{ij} are quite small, e.g. the second largest value is $C_{22} = 99$ GPa and the third largest value is $C_{11} = 22$ GPa. The trend $C_{33} \gg C_{22} > C_{11}$ is consistent with the $\xi_1 \gg \xi_2 > \xi_3$ trend in the linear thermal expansion components (see figure 6) as well as the (relative) charge density distribution shown

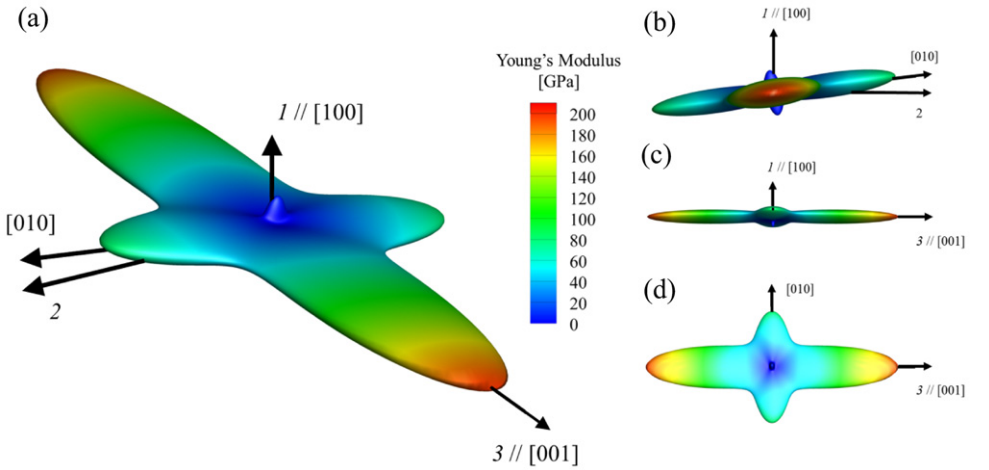

Figure 8. (*a*) Young's modulus (E) surface for cellulose I_β computed at 300 K. Each point on the given surface represents the magnitude of Young's modulus in the direction of a vector from the origin to the point; the color map clearly reveals the Young's modulus variation and emphasizes the extreme anisotropy of the system. The symbol // in this figure means 'parallel to'. (*b*)–(*d*) These show additional views of the surface in (*a*).

in figure 3. Moreover, these trends are consistent with the strong bonding along the c axis direction in cellulose I_β, and weaker interaction along the a axis direction, as discussed above (see also figure 1(*a*)). The large difference between different C_{ij} values is also suggestive of the extreme elastic anisotropy of cellulose I_β. Table 2 also lists some representative values of axial and transverse elastic modulus. While the experimental axial elastic modulus can be compared with $E_{33} = 1/S_{33}$, none of the experimental techniques are sensitive enough to separate out the specific transverse orientations which prevent us for making direct comparisons between experiments and our predicted values (e.g. E_{11}, E_{22}).

To more thoroughly characterize the extreme anisotropies suggested by the C_{ij}, we plotted the variation of the Young's modulus along different directions. Figure 8(*a*) depicts a 3D representation of Young's modulus for crystalline cellulose computed at 300 K along three crystallographic directions. The shape of this surface is indicative of the anisotropy of cellulose I_β (an isotropic material would have a perfectly spherical Young's modulus surface). The distance between each point on the surface and the origin represents the magnitude of the Young's modulus in the direction of the vector from the origin to the surface point. The Young's modulus variation is also mapped by color onto the surface to emphasize the extreme anisotropy of cellulose I_β. Additional views are shown in figures 8(*b*)–(*d*).

Two-dimensional polar plots of the variation of Young's modulus with respect to selected crystallographic planes and at different temperatures can also be generated. Figure 9 shows such a plot which depicts the variation of Young's moduli E_{11} and E_{33} in the 1–3 plane with the orientation angle (θ), considering the 2 axis as the rotation axis. The Young's modulus is shown for $T = 0$, 300 and 500 K. Clearly the Young's modulus in all directions considered does not significantly change with T. The direction defined by the 3 axis (c axis, see figure 2) exhibits the highest value of Young's modulus, varying from 202 GPa at 0 K to 196 GPa at 300 K and down to 190 GPa at 500 K. This variation in Young's modulus between 0 and 500 K represents a 6.1% variation with respect to the 300 K value. It is important to note that a deviation of only 10° with respect to the longitudinal alignment (c axis) will reduce the

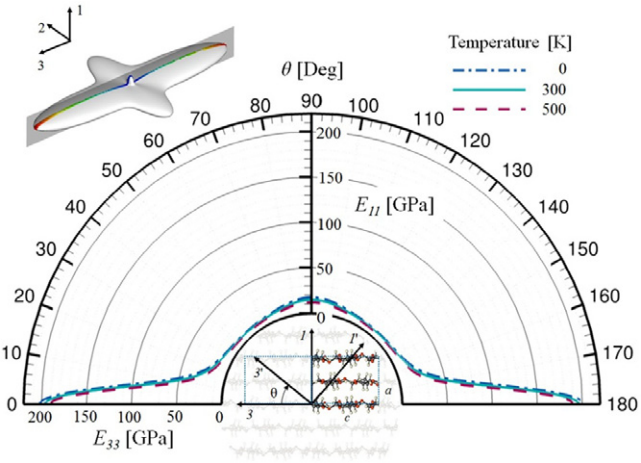

Figure 9. Polar plot showing the Young's moduli (E_{11} and E_{33}) as a function of the rotation angle (θ) for $T = 0$ K (dotted–dashed curve), $T = 300$ K (solid curve), and $T = 500$ K (dashed curve). The 2 axis (pointing into the page) is considered to be the rotation axis. The value of either modulus for a given direction can be read directly from the figure by defining a straight line from the origin to the desired curve.

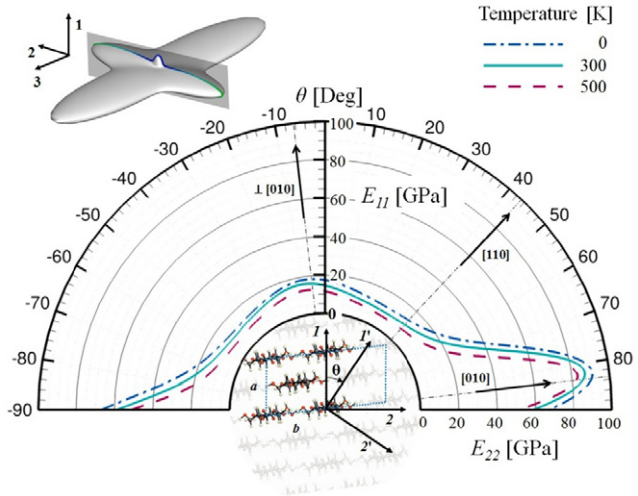

Figure 10. Polar plot showing the Young's moduli (E_{11} and E_{22}) as a function of the rotation angle (θ) for $T = 0$ K (dotted–dashed curve), $T = 300$ K (solid curve) and $T = 500$ K (dashed curve), along the plane depicted at the upper left-hand corner. The 3 axis (pointing into the page) is considered to be the rotation axis. The value of either modulus for a given direction can be read directly from the figure by defining a straight line from the origin to the desired curve.

theoretical Young modulus from approximately 200 to 70 GPa. This important reduction in the stiffness is attributed to the contribution of the weak interaction between layers along the a axis, which are mainly dominated by vdW forces, as the load deviates from the a direction. These deformation mechanisms have been previously discussed in [47].

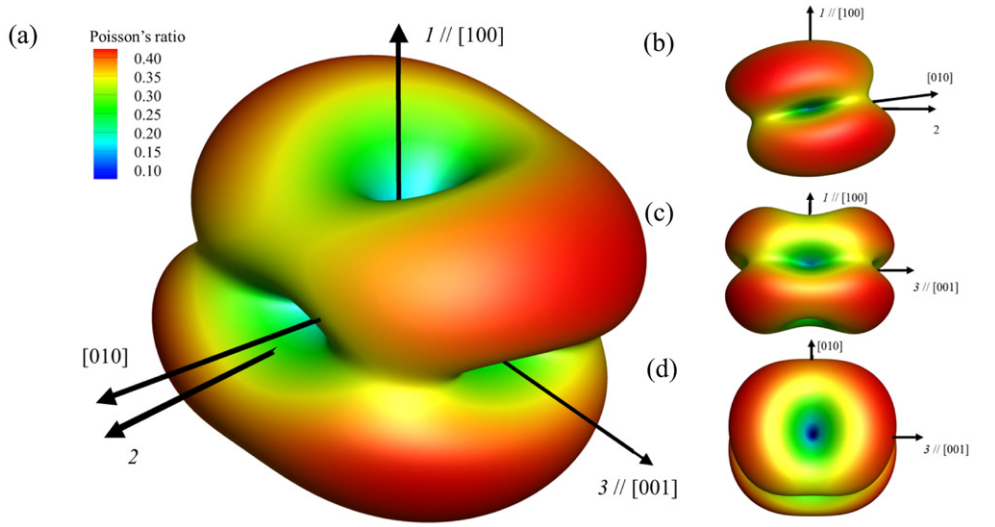

Figure 11. (*a*) Average Poisson's ratio surface for cellulose I_β computed at 300 K. Each point on the given surface represents the magnitude of Poisson's ratio in the direction of a vector from the origin to the point; the color map helps identifying the Poisson's ratio variation and emphasizes the extreme anisotropy of the system. (*b*)–(*d*) These show additional views of the surface in (*a*).

A similar analysis was performed where the angular variations of Young's moduli E_{11} and E_{22} were analyzed over the 1–2 plane. The resulting polar plot is shown in figure 10, The highest values of the Young's modulus E_{22} occurs along the [0 1 0] directions (*b* axis) in the plane with values of 91 GPa at 0 K, 87 GPa at 300 K and 83 GPa at 500 K. Although the variation in Young's modulus between 0 and 500 K is 8 GPa (as opposed to 12 GPa along the *c* axis), it represents a 9.2% variation with respect to its value at 300 K. This is the reason why figure 10 seems to show a larger difference between temperatures than that considered in figure 9. Also, a more noticeable decrease in the Young's moduli with increasing temperature is evident in figure 9.

The relatively high value of the Young modulus in the [0 1 0] direction with respect to any other direction on the 1–2 plane can be attributed to the hydrogen bond network present in between cellulose chains. Stretching in the [0 1 0] direction implies increasing the in-plane separation of the chains, which has direct impact over the inter-chain hydrogen bonds. A second relative maximum is found in the direction marked as $\perp$[0 1 0] in figure 10. We surmise that this can be explained by the relatively weak vdW forces that govern the response of the system in this direction. The lowest values of Young's modulus are found to be 12 GPa at 0 K, 9 GPa at 300 K and 7 GPa at 500 K. Our computed results are consistent with reported experimental values [19,21–27, 88] and other numerical simulations [20, 23, 47, 89].

Variations of Poisson's ratio were computed and displayed as a surface by applying the same procedure as that used to compute the Young's modulus surface. Since Poisson's ratio is the negative ratio of transverse to axial strain, its interpretation is not as straightforward as Young's modulus. Figure 11(*a*) shows the average Poisson's ratio [47] as a function of any arbitrary orientation computed at 300 K. The extreme anisotropies observed in crystalline cellulose are once again revealed, this time by extreme variations of the average Poisson's ratio. Figure 11(*a*) shows that the lowest value of the average Poisson's ratio ($\sim$0.1) occurs

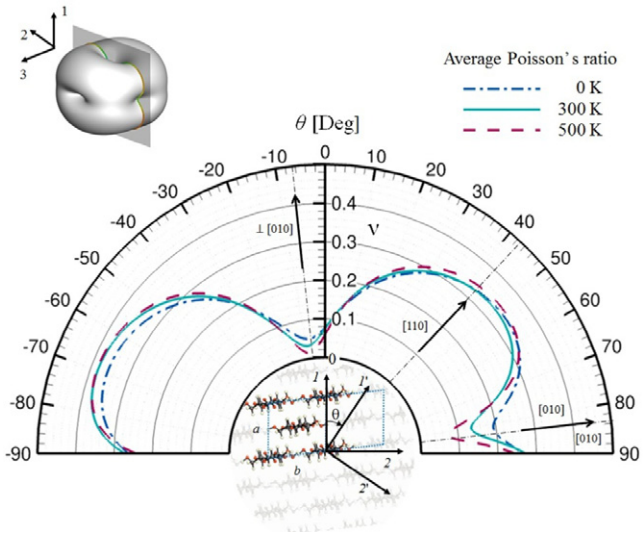

Figure 12. Polar plot showing the average Poisson's ratio as a function of the rotation angle (θ) for $T = 0$ K (dotted–dashed curve), $T = 300$ K (solid curve), and $T = 500$ K (dashed curve), along the plane depicted at the upper left-hand corner. The 3 axis (pointing in and out of the page) is considered to be the rotation axis; the value of Poisson's ratio for a given direction can be read directly from the figure by defining a straight line from the origin to the desire angle.

Table 3. Calculated thermal conductivity of cellulose I_β obtained using RNEMD with the pcff+ force field in LAMMPS at room temperature (298 K). Note that λ_1, λ_2 and λ_3 correspond to the directions along the cellulose I_β structure indicated in figures 1 and 2.

Method	λ_1 (W m^{-1} K^{-1})	λ_2 (W m^{-1} K^{-1})	λ_3 (W m^{-1} K^{-1})
pcff+, this study	0.24 ± 0.05	0.52 ± 0.05	0.90 ± 0.06

along the main crystallographic directions denoted in the figure, whereas the extreme value of 0.4 occurs along other directions. Note that figures 11(*b*)–(*d*) show alternate views of the surface in figure 11(*a*).

Figure 12 is a polar plot that shows the variation of the average Poisson's ratio, ν, over the 1–2 plane for $T = 0$, 300 and 500 K. The first relative minimum can be found in the [0 1 0] direction (*b* axis, right-hand corner of the figure). As the temperature increases, Poisson's ratio decreases along [0 1 0] suggesting a reduction in the effects of separate cellulose chains over the final shape of the crystal. A similar behavior is found in the direction marked as $\perp$[0 1 0], where vdW interactions govern the elastic response of the material. For [1 1 0], temperature appears to have no effect over Poisson's ratio. Comparison with previous publications [23, 47, 84, 89] shows results that are in good agreement with the values reported in this study.

4.5. Thermal conductivity

Table 3 summarizes the predicted thermal conductivity values λ_1, λ_2 and λ_3 of cellulose I_β. These results were obtained in terms of the RNEMD simulations using the pcff+ [90]

force field, and the molecular dynamics simulation code LAMMPS [91] within the MedeA framework [92].

Due to a limitation in the LAMMPS code (the molecular dynamics code employed in the present study), it was convenient to perform these calculations based on an orthorhombic cell with axes 1, 2 and 3 (as indicated in figures 1 and 2). This was achieved using a unit cell with eight times the volume of the conventional cell mentioned in section 3.1. Inspection of the lattice shows that the following transformation yields an almost exactly orthorhombic cell:

$$\begin{aligned} a' &= a \\ b' &= -a + 8 \cdot b \\ c' &= c, \end{aligned} \tag{6}$$

where a, b and c are the original lattice vectors of the cellulose I_β ($P2_1$) structure (see figure 1) and a', b' and c' are the lattice vectors of the orthorhombic cell. Adjusting the resulting cell to be perfectly orthorhombic effectively fixes the cell angle γ at 96.67°, which is within a fraction of a degree of that found in this study and from experiment, as shown in table 1. The lattice parameters used for these calculations, which came from initial DFT calculations, were $a = 7.563$ Å, $b = 8.133$ Å, $c = 10.395$ Å, $\alpha = \beta = 90°$ and $\gamma = 96.67°$. This resulted in an orthorhombic cell with $a' = 7.563$ Å, $b' = 64.621$ Å and $c' = 10.395$ Å. In order to validate the force field, we evaluated pcff+ relative to DFT results. We found that most of the 0 K lattice parameters from LAMMPS/RNEMD with the pcff+ force field are within 0.5% of the values predicted with the DFT method. A comparison of the 0 K values may be found in table S6 of the online supplementary material (stacks.iop.org/MSMSE/22/085012/mmedia). Calculated 0 K results from LAMMPS/RNEMD with the pcff+ force field (based on the energy–volume EOS without the ZPE correction) are listed in table S6 of the online supplementary material. Note that γ is slightly overpredicted by LAMMPS/RNEMD with the pcff+ force field by only 1.83%. The temperature-dependent lattice constants from LAMMPS/RNEMD with the pcff+ force field are also listed in table S7 of the online supplementary material (stacks.iop.org/MSMSE/22/085012/mmedia) at selected temperatures between 0 and 500 K. These values are compared with DFT-D2 values at 0 K.

As mentioned previously, the simulation cell for LAMMPS/RNEMD calculations must be reasonably large in the direction of the measurement because it must be subdivided into layers for the measurement of the temperature profile. For each of the three Cartesian directions, a supercell based on the orthorhombic cell with a dimension in the direction of interest between 60 and 70 Å was constructed and used for the LAMMPS/RNEMD calculations. For direction 1, a $9 \times 1 \times 1$ supercell with an extent in 1 of 68.068 Å, containing 6048 atoms was used. In direction 2, a $1 \times 1 \times 6$ supercell with an extent of 62.371 Å and 4032 atoms was used. In direction 3, the original orthorhombic cell with an extent of 64.621 Å and 672 atoms was used. For each simulation, the system was thermally equilibrated using *NVT* (N: number of particles, V: volume and T: temperature) dynamics for 50 ps, and then constant energy (*NVE*) dynamics was applied, during which the RNEMD was carried out by swapping momenta of one pair of particles every 600 steps for the direction 1, 200 steps for the direction 2 and 250 steps for the direction 3. For the directions 1 and 2, a total time of 2 ns was simulated during this phase, using a 1 fs time step. The simulation in the direction 3 was more sensitive, perhaps because of the small system size, so it was simulated for 1 ns using a 1 fs time step. The cell was divided into 30 layers in the direction of the heat flow for the measurement of the temperature. The temperatures of the hot and cold layers and the

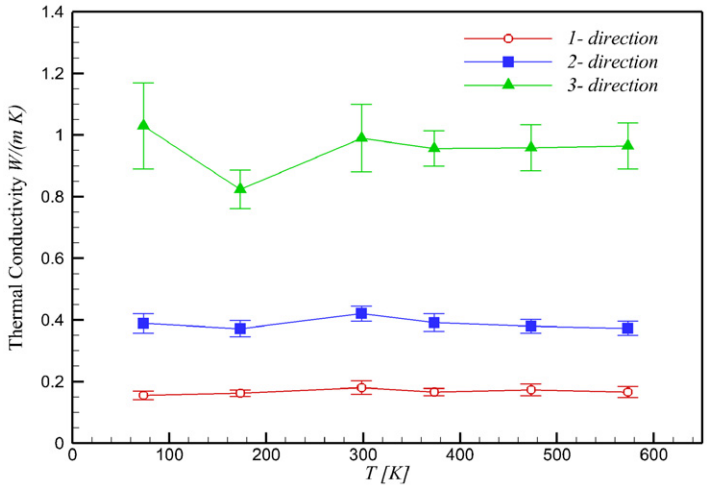

Figure 13. Calculated thermal conductivity (λ_i) as a function of T for the 73–573 K range.

two adjacent layers were not used to fit the temperature profile since non-linear effects are often observed close to where the system is being driven. This left 24 layers for which the temperature was measured, from which the slope was obtained using a linear least-squares fit. The error bars were obtained from a statistical analysis of the points, and reflect a 95% level of certainty.

Figure 13 shows the RNEMD-predicted variation of the thermal conductivity values in directions 1, 2 and 3 with T from 73 to 473 K. Note that no experimental thermal conductivity data for the cellulose I_β structure could be located in the literature. The temperature dependence of the thermal conductivity was calculated in a similar way to the initial calculations outlined above. Because of the sensitivity in the 2 direction previously noted, a $2 \times 1 \times 2$ supercell of the initial orthorhombic supercell was used, with $a = 15.126$ Å and $c = 20.780$ Å to start and 2688 atoms. With this cell, a time step of 1 fs was found to be reasonable. The number of steps between swapping momenta was adjusted based on the initial results to produce a reasonable temperature difference and improve the statistical accuracy of the results. The final rates were one swap in 400 steps for direction 1, one swap in 250 for direction 2 and one swap in 200 for direction 3. At each temperature, the cell was equilibrated using 400 ps of *NPT* dynamics (P: pressure) with the lengths of the cell allowed to fluctuate but with the angles fixed at 90°. The cell was then adjusted to an average value and the thermal conductivity measured using RNEMD with a constant energy ensemble, sampling over 2 ns after equilibrating the temperature for 200 ps using *NVT* dynamics. The density for the cells used in directions 1 and 2 equilibrated to essentially the same value within the statistical errors. However, the cell used for extracting the thermal conductivity in direction 3 constantly underwent a phase transformation to a different structure of cellulose, perhaps due to the shape of the cell emphasizing certain directions or perhaps due to limitations in the accuracy of the force field. To avoid this transformation, the cell was fixed (i.e. isotropically expanded or contracted) to the density obtained at each temperature from the calculations for the 1 and 2 directions. Note the larger standard deviations for this direction, presumably because the chains are moving much more due to the incipient phase transformation even though the cell is fixed in the calculation. As can be seen in figure 13, the thermal conductivity in each direction is independent of the

temperature to within the statistical accuracy. The values are slightly different from those in table 3 due to the volume relaxation. The density of the sample used in the initial calculations at 298 K was 1.696 g ml^{-1}. That predicted by the pcff+ force field at the same temperature is about 1.61 g ml^{-1}.

The results in table 3 and figure 13 are consistent with the results for ξ_i and also the bonding patterns in the cellulose I_β structure. The thermal conductivity is largest along direction 3, which is along the molecular chains (see figures 1 and 2). This is the direction of the strongest bonding and the lowest thermal expansion. In direction 2, which is roughly the direction of the hydrogen bonded network, the thermal conductivity is intermediate, as is the thermal expansion. In direction 1, which corresponds to the weak vdW interactions between the sheets of cellulose, the thermal conductivity is quite low and the thermal expansion is large.

5. Summary

In terms of the van der Waals density functional, i.e. the PBE-D2 method, the extreme anisotropies of the thermal expansion and elastic properties have been predicted for native cellulose I_β. With this new modeling capability, this study was able to develop new knowledge on the temperature dependence and anisotropy of the elastic and thermal properties of cellulose I_β. It is found that the PBE-D2 method satisfactorily describes the three-dimensional structural properties as well as the phonon, thermodynamic, and elastic properties of cellulose I_β. For instance, our predictions at 0 K are well below 0.5% from the experimental values obtained at 15 K [55]. Similarly, the predicted lattice parameters a, b, c and (cell angle) γ of cellulose I_β as a function of temperature yielded very reasonable results compared with the scattered experimental data. The temperature variations of H, S and C_p were in close accord with experimental data. The room temperature values of H, S and C_p fall between 7.5% with respect to the experimental data (table S1).

Calculations of the elasticity tensor, C_{ij}, showed that C_{33} is the largest of the elastic stiffness matrix components, followed by a moderate C_{22}, and then a small C_{11}. Other C_{ij} of the monoclinic cellulose I_β are all quite small ($<C_{11}$). The large difference between the C_{ij} is indicative of the extreme elastic anisotropy in the cellulose I_β structure; this is clearly evident in the computed direction-dependent Young's modulus and Poisson's ratio plots. At finite temperatures, thermodynamic properties predicted via the first-principles quasi-harmonic approach are in reasonable accord with available measurement data, such as entropy, enthalpy, and constant pressure heat capacity. Regarding the thermal expansion coefficients, ξ_i, we find that ξ_1 is the largest, whereas ξ_2 and especially ξ_3 are quite small. These values are consistent with the scarce experimental data and suggest a strong correlation between the high elastic modulus and low axial thermal expansion of cellulose I_β compared with other polymers.

The predicted results, such as the large ξ_1 and C_{33}, and the quick decrease of C_{11} with respect to temperature, are traceable to the weak van der Waals force between layers perpendicular to the a axis direction and the strong hydrogen bond along the b axis direction. These features of cellulose I_β can be viewed quantitatively by the stretching force constants between atomic pairs and qualitatively by the relative charge density, i.e. the charge gain or loss. The calculated thermal conductivity values are consistent with the thermal expansion coefficients and the bonding patterns in the structure. We note that the thermal conductivity has its maximum along the c axis direction (0.90 ± 0.06 W m^{-1} K^{-1}), where the strongest bonds are present, and its lowest values in the a and b axis directions. In general, the thermal

conductivity of native cellulose I_β shows minimal sensitivity to temperature over the 73–573 K range considered in this study.

Acknowledgments

The authors acknowledge the staff of the High Performance Computing Center at General Motors. Additional computational resources, networking and support were provided by GM Information Systems and Services. SLS and ZKL acknowledge support from the National Science Foundation through grant Nos CMMI-1333999 and CHE-1230924. Also, RJM and PDZ are grateful for financial support by the Forest Products Laboratory under USDA grant 07-CR-11111120-093, the Purdue Research Foundation and National Science Foundation through grant No CMMI-1131596.

Appendix A. Additional details on methods and codes used in this study

All DFT calculations with the VASP 5.2.12 code [59, 60] used the vdW corrections and PBE-D2 [63]. The structure of cellulose I_β (space group $P2_1$) shown in figure 1 was constructed using the *Crystalline Cellulose-Atomistic Toolkit* [57] in NanoHUB.org, which is publicly available. For the Phonon calculations, total energies were calculated for the relaxed cellulose I_β structure by integrating over a Monkhorst–Pack mesh of $k-$points in the Brillouin zone with the linear tetrahedron method with Blöchl corrections. The plane-wave cutoff energy for all calculations was 500 eV. Phonon calculations were based upon the supercell method using the Parlinski PHONON code, as implemented in the MedeA environment [70, 71], with VASP as the computational engine. More details about phonon calculations using the PHONON code as implemented in MedeA can be found in [38, 50, 66].

The unique components of the stiffness matrix, C_{ij}, were computed within the MedeA environment using the strain–stress method as developed by Le Page and Saxe [64, 65]. The C_{ij} were directly computed from the first derivatives of the VASP-computed cell stresses for selected applied strains. This method avoids the numerical difficulties often encountered with evaluations of the second derivatives of the total (electronic) energy with respect to strain, and reduces the number of required VASP calculations. The C_{ij} are sensitive to the k-point mesh, and this required a series of ancillary calculations to test k-point convergence of each of the 13 unique C_{ij} for the monoclinic cellulose I_β structure: the $7\times7\times7$ k-point mesh was found to be sufficient. In addition, it was determined that the application of four successive strains, namely, 0.5%, 1.0%, 1.5% and 2.0% was adequate to obtain $\leqslant$1.0% statistical error in each C_{ij}. The quality of the least-squares fit, as gauged by the computed least-squares residual, was $\leqslant$1.0% for all calculations. The small residuals are consistent with negligible anharmonic effects in the computed C_{ij} due to the applied strains. Once the stiffness matrix was computed, it was subsequently inverted to obtain the compliance matrix, S_{ij}. It should be kept in mind that the C_{ij} and the S_{ij} depend on the definition of the coordinate system chosen for the simulations. More details about the elastic calculations using the Le Page and Saxe method as implemented in MedeA can be found in [38, 50, 66–69]. Details on how the stiffness and compliance matrix are obtained for crystalline cellulose at 0 K can be found in [47]. Seven E–V data points were used to fit the EOS (equation (2)).

The variation of the Young's modulus along different directions shown in figures 8–12 was computed using the post-processing software *Anisotropy Calculator—3D Visualization Toolkit*, which was specifically developed for this study and it is publicly available in nanoHUB.org [87].

Appendix B. Isentropic and isothermal stiffness components

To calculate the isothermal elasticity tensor components, $C_{ij}^{T}(T)$, we first compute the 0 K C_{ij} at selected volumes above and below the equilibrium volume V_0 at 0 K. Using $V_0(T)$, the $C_{ij}^{T}(T)$ are computed via interpolation from the $C_{ij}(V)$ wherein the volume dependence is eliminated. Here, the kinetic energy and the fluctuations of microscopic stress tensors [93] are ignored. The measured elasticity tensor components at high temperatures (e.g. using the resonance method) are usually isentropic since the system is adiabatic due to the faster speed of elastic waves relative to heat diffusion [39, 52]. The isentropic elasticity tensor is defined as $C_{ij}^{S}(T)$. From Davies [75], the $C_{ij}^{S}(T)$ can be written in terms of the $C_{ij}^{T}(T)$ as

$$C_{ij}^{S}(T) = C_{ij}^{T}(T) + \frac{TV\kappa_i\kappa_j}{C_V}, \tag{B1}$$

where

$$\kappa_i = -\sum_{j=1}^{6}\left(\frac{\partial\sigma_i}{\partial\varepsilon_j}\right)_T\left(\frac{\partial\varepsilon_j}{\partial T}\right)_\sigma = -\sum_{j=1}^{6}\xi_j C_{ij}^{T}(T) \tag{B2}$$

and the reduced forms of stress, strain and linear thermal expansion are denoted by σ_i, ε_j and ξ_j, respectively.

References

[1] Jarvis M 2003 Chemistry—cellulose stacks up *Nature* **426** 611–12
[2] Cabrera R Q, Meersman F, McMillan P F and Dmitriev V 2011 Nanomechanical and structural properties of native cellulose under compressive stress *Biomacromolecules* **12** 2178–83
[3] Klemm D, Heublein B, Fink H P and Bohn A 2005 Cellulose: fascinating biopolymer and sustainable raw material *Angew. Chem. Int. Edn* **44** 3358–93
[4] http://bct.eco.umass.edu/publications/by-title/cellulose-insulation-a-smart-choice/
[5] Baumann M G D and Conner A H 2003 Carbohydrate polymers as adhesives *Handbook of Adhesive Technology* 2nd edn (London: Taylor and Francis) pp 495–510
[6] Zugenmaier P 2006 Materials of cellulose derivatives and fiber-reinforced cellulose–polypropylene composites: characterization and application *Pure Appl. Chem.* **78** 1843–55
[7] www.greencarcongress.com/2013/12/20131220-ford.html
[8] http://sperecycling.org/sites/sperecycling.org/files/papers/GPEC2013/gpec2013-s7-banning.pdf
[9] Cao Y, Zavaterri P, Youngblood J, Moon R and Weiss J 2013 The influence of cellulose nano crystal additions on the performance of cement paste *Cement and Concrete Composites* submitted
[10] Moon R J, Martini A, Nairn J, Simonsen J and Youngblood J 2011 Cellulose nanomaterials review: structure, properties and nanocomposites *Chem. Soc. Rev.* **40** 3941–94
[11] Samir M A S A, Alloin F and Dufresne A 2005 Review of recent research into cellulosic whiskers, their properties and their application in nanocomposite field *Biomacromolecules* **6** 612–26
[12] Klemm D, Kramer F, Moritz S, Lindstrom T, Ankerfors M, Gray D and Dorris A 2011 Nanocelluloses: a new family of nature-based materials *Angew. Chem. Int. Edn* **50** 5438–66
[13] Postek M T, Moon R J, Rudie A and Bilodeau M (ed) 2013 *Production and Applications of Cellulose Nanomaterials* (Peachtree Corners: TAPPI Press)
[14] Oksman K and Sain M (ed) 2006 *Cellulose Nanocomposites: Processing, Characterization and Properties* (*ACS Symposium Series* Book 938) (Washington, DC: American Chemical Society)
[15] Belton P S, Tanner S F, Cartier N and Chanzy H 1989 High-resolution solid-state carbon-13 nuclear magnetic resonance spectroscopy of tunicin, an animal cellulose *Macromolecules* **22** 1615–17
[16] Bucko T, Tunega D, Angyan J G and Hafner J 2011 *Ab initio* study of structure and interconversion of native cellulose phases *J. Phys. Chem.* A **115** 10097–105
[17] Parthasarathi R, Bellesia G, Chundawat S P S, Dale B E, Langan P and Gnanakaran S 2011 Insights into hydrogen bonding and stacking interactions in cellulose *J. Phys. Chem.* A **115** 14191–202

[18] Nishiyama Y, Langan P and Chanzy H 2002 Crystal structure and hydrogen-bonding system in cellulose 1 beta from synchrotron x-ray and neutron fiber diffraction *J. Am. Chem. Soc.* **124** 9074–82
[19] Wagner R, Moon R, Pratt J, Shaw G and Raman A 2011 Uncertainty quantification in nanomechanical measurements using the atomic force microscope *Nanotechnology* **22** 455703
[20] Wu X, Moon R J and Martini A 2013 Crystalline cellulose elastic modulus predicted by atomistic models of uniform deformations and nanoscale indentation *Cellulose* **20** 43–55
[21] Sakurada I, Nukushina Y and Ito T 1962 Experimental determination of the elastic modulus of crystalline regions in oriented polymers *J. Polym. Sci.* **57** 651–60
[22] Sakurada I, Ito T and Nakamae K 1964 Elastic moduli of polymer crystals for the chain axial direction *Die Makromol. Chem.* **75** 1–10
[23] Matsuo M, Sawatari C, Iwai Y and Ozaki F 1990 Effect of orientation distribution and crystallinity on the measurement by x-ray diffraction of the crystal lattice moduli of cellulose I and II *Macromolecules* **23** 3266–75
[24] Nishino T, Takano K and Nakamae K 1995 Elastic modulus of the crystalline regions of cellulose polymorphs *J. Polym. Sci.* B **33** 1647–51
[25] Ishikawa A, Okano T and Sugiyama J 1997 Fine structure and tensile properties of ramie fibres in the crystalline form of cellulose I, II, IIII and IVI *Polymer* **38** 463–8
[26] Diddens I, Murphy B, Krisch M and Müller M 2008 Anisotropic elastic properties of cellulose measured using inelastic x-ray scattering *Macromolecules* **41** 9755–9
[27] Lahiji X, Xu X, Reifenberger R, Raman A, Rudie A and Moon R J 2010 Atomic force microscopy characterization of cellulose nanocrystals *Langmuir* **26** 4480–8
[28] Hidaka H, Kim U-J and Wada M 2010 Synchrotron x-ray fiber diffraction study on the thermal expansion behavior of cellulose crystals in tension wood of Japanese poplar in the low-temperature region *Holzforschung* **64** 167–71
[29] Hori R and Wada M 2005 The thermal expansion of wood cellulose crystals *Cellulose* **12** 479–84
[30] Wada M 2002 Lateral thermal expansion of cellulose I-beta and IIII polymorphs *J. Polym. Sci.* B **40** 1095–102
[31] Wada M, Hori R, Kim U-J and Sasaki S 2010 X-ray diffraction study on the thermal expansion behavior of cellulose I beta and its high-temperature phase *Polym. Degradation Stab.* **95** 1330–4
[32] Bergenstrahle M, Berglund L A and Mazeau K 2007 Thermal response in crystalline I beta cellulose: a molecular dynamics study *J. Phys. Chem.* B **111** 9138–45
[33] Kulasinski K, Keten S, Churakov S V, Derome D and Carmeliet J 2014 A comparative molecular dynamics study of crystalline, paracrystalline and amorphous states of cellulose *Cellulose* **21** 1103–16
[34] Diaz J A, Wu X, Martini A, Youngblood J P and Moon R 2013 Thermal expansion of self-organized and shear-oriented cellulose nanocrystal films *Biomacromolecules* **14** 2900–8
[35] Hatakeyama T, Nakamura K and Hatakeyama H 1982 Studies on heat capacity of cellulose and lignin by differential scanning calorimetry *Polymer* **23** 1801–4
[36] Hatakeyama T and Hatakeyama H 2004 *Thermal Properties of Green Polymers and Biocomposites* vol 4 (Berlin: Springer)
[37] Shang S L, Wang Y, Kim D and Liu Z K 2010 First principles thermodynamics from phonon and Debye model: application to Ni and Ni_3Al *Comput. Mater. Sci.* **47** 1040–8
[38] Wrobel J, Hector L G Jr, Wolf W, Shang S L, Liu Z K and Kurzydlowski K J 2012 Thermodynamic and mechanical properties of lanthanum–magnesium phases from density functional theory *J. Alloys Compounds* **512** 296–310
[39] Shang S L, Zhang H, Wang Y and Liu Z K 2010 Temperature-dependent elastic stiffness constants of alpha- and theta-Al_2O_3 from first principles calculations *J. Phys.: Condens. Matter* **22** 375403
[40] Shimazaki Y, Miyazaki Y, Takezawa Y, Nogi M, Abe K, Ifuku S and Yano H 2007 Excellent thermal conductivity of transparent cellulose nanofiber/epoxy resin nanocomposites *Biomacromolecules* **8** 2976

[41] Hatta I, Sasuga Y, Kato R and Maesono A 1985 Thermal diffusivity measurement of thin films by means of an ac calorimetric method *Rev. Sci. Instrum.* **56** 1643–7
[42] Hashimoto T, Matsui Y, Hagihara A and Miyamoto A 1990 Thermal diffusivity measurement of polymer films by the temperature wave method using Joule-heating *Thermochim. Acta* **163** 317–24
[43] Gheribi A E and Chartrand P 2013 An *in silico* method to predict the thermal conductivity in insulating crystals *Proc. 31st Int. Thermal Conductivity Conf.* pp 299–306
[44] Stackhouse L and Stixrude L 2009 Thermal conductivity of MgO and $MgSiO_3$ perovskite at lower mantle conditions *American Geophysical Union, Fall Meeting (San Francisco, December 2009)*
[45] De Koker N 2009 Thermal conductivity of MgO periclase from equilibrium first principles molecular dynamics *Phys. Rev. Lett.* **103** 125902
[46] Chen M X and Podlucky R 2013 Electronic thermal conductivity as derived by density functional theory *Phys. Rev.* B **88** 045134
[47] Dri F, Hector L H Jr, Moon R J and Zavattieri P D 2013 Anisotropy of the elastic properties of crystalline cellulose I_β from first principles density functional theory with van der Waals interactions *Cellulose* **20** 2703–18
[48] Grimme S 2006 Semiempirical GGA-type density functional constructed with a long-range dispersion correction *J. Comput. Chem.* **27** 1787–99
[49] Shang S L, Wang Y and Liu Z K 2007 First principles calculations of phonon and thermodynamic properties in the boron–alkaline earth metal binary systems: B–Ca, B–Sr, and B–Ba *Phys. Rev.* B **75** 024302
[50] Shang S L, Hector L G Jr, Shi S Q, Qi Y, Wang Y and Liu Z K 2012 Lattice dynamics, thermodynamics and elastic properties of monoclinic Li_2CO_3 from density functional theory *Acta Mater.* **60** 5204–16
[51] Wang Y, Liu Z K and Chen L Q 2004 Thermodynamic properties of Al, Ni, NiAl, and Ni_3Al from first principles calculations *Acta Mater.* **52** 2665–71
[52] Wang Y, Wang J J, Zhang H, Manga V R, Shang S L, Chen L Q and Liu Z K 2010 A first principles approach to finite temperature elastic constants *J. Phys.: Condens. Matter* **22** 225404
[53] Mavromaras A, Rigby D, Wolf W, Christensen M, Halls M, Freeman C, Saxe P and Wimmer E 2010 Computational materials engineering: capabilities of atomic-scale prediction of mechanical, thermal, and electrical properties of microelectronic materials *11th Int. Conf. on Thermal, Mechanical and Multiphysics Simulation and Experiments in Micro-Electronics and Micro-Systems, EuroSimE* (Bordeaux, April 2010) pp 78–87
[54] Nishiyama Y, Sugiyama J, Chanzy H and Langan P 2003 Crystal structure and hydrogen bonding system in cellulose I_α from synchrotron x-ray and neutron fiber diffraction *J. Am. Chem. Soc.* **125** 14300–6
[55] Nishiyama Y, Johnson G P, French A D, Forsyth V T and Langan P 2008 Neutron crystallography, molecular dynamics, and quantum mechanics studies of the nature of hydrogen bonding in cellulose I-beta *Biomacromolecules* **9** 3133–40
[56] O'Sullivan A C 1997 *Cellulose: the structure slowly unravels* **4** 173–207
[57] Zuluaga M G, Dri F L, Moon R J and Zavattieri P D 2013 Crystalline cellulose-atomistic toolkit, https://nanohub.org/tools/ccamt, DOI:10.4231/D35T3G03B
[58] Matthews J F, Beckham G T, Bergenstråhle-Wohlert M, Brady J W, Himmel M E and Crowley M F 2012 Comparison of cellulose I_β simulations with three carbohydrate force fields *J. Chem. Theory Comput.* **8** 735–48
[59] Kresse G and Furthmuller J 1996 Efficient iterative schemes for *ab initio* total-energy calculations using a plane-wave basis set *Phys. Rev.* B **54** 11169–86
[60] Kresse G and Furthmuller J 1996 Efficiency of *ab-initio* total energy calculations for metals and semiconductors using a plane-wave basis set *Comput. Mater. Sci.* **6** 15–50
[61] Kresse G and Joubert D 1999 From ultrasoft pseudopotentials to the projector augmented-wave method *Phys. Rev.* B **59** 1758–75
[62] Perdew J P, Burke K and Ernzerhof M 1996 Generalized gradient approximation made simple *Phys. Rev. Lett.* **77** 3865–8

[63] Bucko T, Hafner J, Lebegue S and Angyan J G 2010 Improved description of the structure of molecular and layered crystals: *ab initio* DFT calculations with van der Waals corrections *J. Phys. Chem.* A **114** 11814–24
[64] Le Page Y and Saxe P 2002 Symmetry-general least-squares extraction of elastic data for strained materials from *ab initio* calculations of stress *Phys. Rev.* B **65** 104104
[65] Le Page Y and Saxe P 2001 Symmetry-general least-squares extraction of elastic coefficients from *ab initio* total energy calculations *Phys. Rev.* B **63** 174103
[66] Shang S L, Hector L G, Wang Y, Zhang H and Liu Z K 2009 First principles study of elastic and phonon properties of the heavy fermion compound CeMg *J. Phys.: Condens. Matter* **21** 246001
[67] Hector L G Jr, Herbst J F, Wolf W, Saxe P and Kresse G 2007 *Ab initio* thermodynamic and elastic properties of alkaline-earth metals and their hydrides *Phys. Rev.* B **76** 014121
[68] Hector L G Jr, Herbst J F and Capehart T W 2003 Electronic structure calculations for LaNi(5) and LaNi(5)H(6): energetics and elastic properties *J. Alloys Compounds* **353** 74–85
[69] Qi Y and Hector L G Jr 2007 Planar stacking effect on elastic stability of hexagonal boron nitride *Appl. Phys. Lett.* **90** 081922
[70] Parlinski K, Li Z Q and Kawazoe Y 1997 First principles determination of the soft mode in cubic ZrO_2 *Phys. Rev. Lett.* **78** 4063–6
[71] Parlinski K 2008 *Software PHONON as Implemented in MedeA 2.8* (Angel Fire, NM: Materials Design)
[72] Shang S L, Wang Y, Mei Z G, Hui X D and Liu Z K 2012 Lattice dynamics, thermodynamics, and bonding strength of lithium-ion battery materials Li*M*PO(4) (M = Mn, Fe, Co, and Ni): a comparative first principles study *J. Mater. Chem.* **22** 1142–9
[73] Bower A F 2011 *Applied Mechanics of Solids* (Boca Raton, FL: CRC Press)
[74] Jones R M 1975 *Mechanics of Composite Materials* vol 2 (London: Taylor and Francis)
[75] Davies G F 1974 Effective elastic-moduli under hydrostatic stress: I. Quasi-harmonic theory *J. Phys. Chem. Solids* **35** 1513–20
[76] Muller-Plathe F and Reith D 1999 Cause and effect reversed in non-equilibrium molecular dynamics: an easy route to transport coefficients *Comput. Theor. Polym. Sci.* **9** 203–9
[77] Li Y, Lin M and Davenport J W 2011 *Ab initio* studies of cellulose I: crystal structure, intermolecular forces, and interactions with water *J. Phys. Chem.* C **115** 11533–9
[78] Shang S L, Wang J, Wang Y, Du Y and Liu Z K 2011 Phonon and thermodynamic properties of Al–Mn compounds: a first principles study *Comput. Mater. Sci.* **50** 2096–103
[79] Oh S Y, Yoo D I, Shin Y, Kim H C, Kim H Y, Chung Y S, Park W H and Youk J H 2005 Crystalline structure analysis of cellulose treated with sodium hydroxide and carbon dioxide by means of x-ray diffraction and FTIR spectroscopy *Carbohydrate Res.* **340** 2376–91
[80] Blokhin A V, Voitkevich O V, Kabo G J, Paulechka Y U, Shishonok M V, Kabo A G and Simirsky V V 2011 Thermodynamic properties of plant biomass components. Heat capacity, combustion energy, and gasification equilibria of cellulose *J. Chem. Eng. Data* **56** 3523–31
[81] Herbst J F and Hector L G Jr 2006 Electronic structure and energetics of the quaternary hydride $Li_4BN_3H_{10}$ *Appl. Phys. Lett.* **88** 231904
[82] Iwamoto S, Kai W H, Isogai A and Iwata T 2009 Elastic modulus of single cellulose microfibrils from tunicate measured by atomic force microscopy *Biomacromolecules* **10** 2571–6
[83] Sturcova A, Davies G R and Eichhorn S J 2005 Elastic modulus and stress-transfer properties of tunicate cellulose whiskers *Biomacromolecules* **6** 1055–61
[84] Nakamura K, Wada M, Kuga S and Okano T 2004 Poisson's ratio of cellulose I-beta and cellulose II *J. Polym. Sci.* B **42** 1206–11
[85] Shang S L, Saengdeejing A, Mei Z G, Kim D E, Zhang H, Ganeshan S, Wang Y and Liu Z K 2010 First principles calculations of pure elements: equations of state and elastic stiffness constants *Comput. Mater. Sci.* **48** 813–26
[86] Simmons G and Wang H 1971 *Single Crystal Elastic Constants and Calculated Aggregate Properties* (Cambridge, MA: MIT Press)

[87] Zuluaga M G, Dri F L, Moon R J and Zavattieri P D 2013 Anisotropy calculator—3D visualization toolkit, https://nanohub.org/resources/matrix2surface, Doi:10.4231/D3K06X13R
[88] Pakzad A, Simonsen J, Heiden P A and Yassar R S 2012 Size effects on the nanomechanical properties of cellulose I nanocrystals *J. Mater. Res.* **27** 528–36
[89] Eichhorn S J and Davies G R 2006 Modelling the crystalline deformation of native and regenerated cellulose *Cellulose* **13** 291–307
[90] 2012 pcff+ forcefield, Materials Design Inc., Santa Fe, NM
[91] Plimpton S 1995 Fast parallel algorithms for short-range molecular dynamics *J. Comput. Phys.* **117** 1–19
[92] 2012 MedeA v2.11, Materials Design, Inc., Santa Fe, NM
[93] Lutsko J F 1989 Generalized expressions for the calculation of elastic constants by computer simulation *J. Appl. Phys.* **65** 2991